24	25	26	27	28	8
Cr	**Mn**	**Fe**	**Co**	**Ni**	**O**
Chromium	Manganese	Iron	Cobalt	Nickel	Oxygen

ROYAL SOCIETY
OF CHEMISTRY

PAPER
Kazuya Kobiro *et al.*
Low-temperature synthesis of porous high-entropy
(CoCrFeMnNi)$_3$O$_4$ spheres and their application to the
reverse water–gas shift reaction as catalysts

Dalton Transactions

PAPER

Check for updates

Low-temperature synthesis of porous high-entropy (CoCrFeMnNi)₃O₄ spheres and their application to the reverse water–gas shift reaction as catalysts†

Ayano Taniguchi, [ID] [a] Takeshi Fujita [ID] [a] and Kazuya Kobiro [ID] *[a,b]

A high-entropy porous spinel oxide [(Co$_{0.2}$Cr$_{0.2}$Fe$_{0.2}$Mn$_{0.2}$Ni$_{0.2}$)$_3$O$_4$] was synthesized *via* a solvothermal method and calcination. Solvothermal conditions yielding homogeneous precursor composites with five metals were optimized. Low-temperature calcination of the amorphous composites at 500 °C for 60 min yielded porous spheres formed by small primary particles, with crystal structures attributed to single-phase spinels. The homogeneity of the five elements in the spheres was verified *via* scanning transmission electron microscopy and energy-dispersive X-ray spectroscopy analysis. The high-entropy (Co$_{0.2}$Cr$_{0.2}$Fe$_{0.2}$Mn$_{0.2}$Ni$_{0.2}$)$_3$O$_4$ spheres exhibited superior catalytic activity and long-term stability for the reverse water–gas shift reaction at 700 °C for at least 15 h. The importance of the Cr component in stabilizing the spinel structure was demonstrated. Mn, Fe, Co, and Ni served as active sites in the reaction. The advantage of solvothermal synthesis for porous high-entropy materials was discussed.

Introduction

High-entropy materials, which typically contain equimolar amounts of five or more elements randomly distributed throughout a single-phase structure, are a new class of functional materials. The concept of "high entropy" was first proposed for alloys in 2004[1,2] and has been used for oxides,[3] nitrides,[4] carbides,[5] borides,[6] *etc.* High-entropy oxides (HEOs) are defined as single-phase solid solutions containing equimolar amounts of more than five cations. HEOs exhibit unique properties such as high structural and thermal stability, as well as lattice distortion effects.[3,7] Hence, their applications as catalysts have been actively studied.

HEOs have been formed primarily *via* solid-state synthesis[8–10] and spray pyrolysis.[11–13] These methods require high temperatures up to 1000 °C and long-time heating processes. The high temperatures lead to crystal growth and, therefore, it is usually difficult to control the morphology, structure, and crystallite size. Typically, the particle size of many HEOs synthesized by high-temperature methods was as

large as several hundred nanometers or one micrometer. Porosity is another important factor for utilization as catalysts and catalyst supports. Thus, low-temperature (<700 °C) synthesis of HEOs has been attracting attention recently. To obtain single-phase HEOs *via* low-temperature calcination, the key has been to prepare a nanocomposite in which the metals are finely mixed at the nanoparticle level, as a precursor before calcination. Liquid-phase syntheses can yield uniformly mixed multiple metal oxides and doped metal oxides.[14,15] Liquid-phase methods such as sol–gels,[16] coprecipitation,[17] and metal–organic frameworks,[18] followed by calcination, have been used for low-temperature HEO synthesis. An HEO prepared by the sol–gel method followed by calcination at 450 °C had a crystallite size of 13 nm with a specific surface area of 20 m^2 g^{-1}.[16] Co-precipitation followed by calcination at 500 °C yielded an HEO with a crystallite size of 30 nm.[17] Notably, the calcination of metal organic frameworks afforded an HEO with an extremely high specific surface area of 206 m^2 g^{-1}.[18] However, little progress has been made in designing their morphologies. Furthermore, synthetic methods can still be improved.

Here, the solvothermal method is discussed, where the sizes and shapes of primary particles and higher-order structures are controllable by adjusting reaction conditions such as metal sources, solvents, additives, and heating.[19–21] Additionally, multiple metal oxides having various crystal structures can be homogeneously mixed at the nanoscale.[22] The present authors have synthesized a variety of metal–oxide

ᵃGraduate School of Engineering, Kochi University of Technology, 185 Miyanokuchi, Tosayamada, Kami, Kochi 782-8502, Japan. E-mail: kobiro.kazuya@kochi-tech.ac.jp
ᵇResearch Center for Structural Nanochemistry, Kochi University of Technology, 185 Miyanokuchi, Tosayamada, Kami, Kochi 782-8502, Japan.
E-mail: kobiro.kazuya@kochi-tech.ac.jp
†Electronic supplementary information (ESI) available. See DOI: https://doi.org/10.1039/d3dt04131j

materials with higher-order spherical morphologies composed of numerous nanoscale primary particles *via* solvothermal methods.[22–26] They exhibited porous structures derived from gaps between the primary particles and high specific surface areas. These features have led to superior catalysts and catalytic supports for various gas-phase reactions.[23,24] These materials have been called micro/mesoporously architected roundly integrated metal oxides (MARIMOs). The synthetic methodology has also been applied to composite MARIMOs, such as SiO_2–TiO_2,[22] TiO_2–Nb_2O_5,[25] and SnO_2-based composites.[26] Therefore, the solvothermal approach could be used for the synthesis of high-entropy MARIMOs (HE-MARIMO) containing five metals.

HEOs have been applied to catalysts for batteries[3,27–30] and electrochemical processes[31–35] such as the oxygen evolution reaction and water oxidation. The structural and thermal stability of HEOs promises gas-phase catalytic reactions at high temperatures; however, there have been limited reports on HEO thermal catalysts for high-temperature gas-phase reactions.[36–38] The reverse water–gas shift (RWGS) reaction converts CO_2 into CO, which can then be converted into hydrocarbons *via* the subsequent Fischer–Tropsch reaction.[39] The RWGS reaction is reversible and endothermic. Furthermore, a high temperature is favored because CH_4 is produced by a side reaction at lower temperatures. Therefore, RWGS reaction catalysts must have excellent high-temperature stability. In this respect, the high-temperature RWGS reaction can be used to evaluate intrinsic HEO properties, such as catalytic activity and stability. Supported metal nanoparticles as catalysts based on noble metals are highly active and selective for RWGS catalysts.[40–43] However, noble metals are scarce and their cost limits large-scale applications, limiting their use to the academic level. Catalysts of commercial interest are $Cu/ZnO/Al_2O_3$ and $FeCrCuO_x$, and more recently also Ni-based catalysts.[44,45] The main challenges of them are poor selectivity in the low temperature regime and stability at high temperatures. Thus, base-metal catalysts for the RWGS reaction that have high activity, stability, and CO selectivity are strongly desired. Spinel oxides containing 3d-transition metals such as Cr, Fe, and Zn are known to work as RWGS reaction catalysts.[46–48] Here, the HEO consisting of five metals (Cr, Mn, Fe, Co, and Ni) was selected as the target material.

In this paper, a novel low-temperature synthetic route for porous and morphology-designed HEOs with a small crystallite size was discussed. The HE-MARIMO with a $(Co_{0.2}Cr_{0.2}Fe_{0.2}Mn_{0.2}Ni_{0.2})_3O_4$ spinel structure was synthesized *via* a two-step process involving a solvothermal synthesis of a precursor composite, followed by calcination at 500 °C for 60 min in air. The resulting composite oxide exhibited nanoscale homogeneity of all five metals. In addition, five different quaternary MARIMOs with one missing element were also synthesized *via* similar methods for comparison. The HE-MARIMO and quaternary MARIMOs were both used as catalysts and their activities were compared with those of a reference composite formed *via* a standard solid-state synthesis. The high-temperature RWGS reaction was selected as a probe reaction to evaluate their catalytic performance and durability. The HE-MARIMO exhibited superior catalytic activity, stability, and CO selectivity relative to the reference composite, and a potential application of the solvothermal reaction to synthesize porous HEOs is discussed.

Experimental

Materials

Chromium(III) nitrate nonahydrate ($Cr(NO_3)_3 \cdot 9H_2O$, 99%) was purchased from Sigma-Aldrich (St Louis, MO, USA). Manganese(II) nitrate hexahydrate ($Mn(NO_3)_2 \cdot 6H_2O$, 98.0%), iron(III) nitrate nonahydrate ($Fe(NO_3)_3 \cdot 9H_2O$, 99.9%), cobalt(II) nitrate hexahydrate ($Co(NO_3)_2 \cdot 6H_2O$, 98.0%), nickel(II) nitrate hexahydrate ($Ni(NO_3)_2 \cdot 6H_2O$, 98.0%), diethylene glycol (diEG), benzoic acid (BA), acetonitrile, and methanol were purchased from FUJIFILM Wako Pure Chemical Corporation (Osaka, Japan). Acetylacetone (acacH), triethylene glycol (triEG), and tetraethylene glycol (tetraEG) were purchased from Tokyo Chemical Industry Co., Ltd (Tokyo, Japan). Cr_2O_3 (99.9%), MnO_2 (99.99%), Fe_2O_3 (99.9%), Co_3O_4 (99.7%), and NiO (99.97%) powders were purchased from Kojundo Chemical Lab. Co., Ltd (Saitama, Japan).

Small-scale preparation of a precursor composite *via* a solvothermal reaction

A methanol/acetonitrile (1/9 (vol/vol)) mixed solution (3.50 mL) with equimolar amounts (70.0 μmol) of $Cr(NO_3)_3 \cdot 9H_2O$, $Mn(NO_3)_2 \cdot 6H_2O$, $Fe(NO_3)_3 \cdot 9H_2O$, $Co(NO_3)_2 \cdot 6H_2O$, and $Ni(NO_3)_2 \cdot 6H_2O$, and triEG (698 μL, 5.25 mmol) was transferred to an SUS-316 high-pressure reactor (10 mL volume). The reactor was heated to 300 °C at a rate of 5.4 °C min^{-1} and the temperature was maintained at 300 °C for 10 min. The reaction was then quenched by placing the reactor in an ice-water bath. The product was collected *via* centrifugation, washed with methanol, and dried under vacuum at 40 °C to yield a powdery material (entry 5 in Table 1). The reaction conditions and yields using other additives and solvents are listed in Table 1.

Large-scale preparation of an HE-MARIMO *via* a solvothermal reaction followed by calcination

A methanol/acetonitrile (1/9 (vol/vol)) mixed solution (35.0 mL) including equimolar amounts (0.700 mmol) of $Cr(NO_3)_3 \cdot 9H_2O$, $Mn(NO_3)_2 \cdot 6H_2O$, $Fe(NO_3)_3 \cdot 9H_2O$, $Co(NO_3)_2 \cdot 6H_2O$, and $Ni(NO_3)_2 \cdot 6H_2O$, and triEG (6.98 mL, 52.5 mmol) was transferred to a high-pressure reactor with an inner Teflon sleeve (100 mL volume). The reactor was heated to 200 °C at a rate of 5.4 °C min^{-1} and the temperature was maintained at 200 °C for 30 min. The reaction was then quenched by placing the reactor in an ice-water bath. The product was collected *via* centrifugation, washed with methanol, and dried under vacuum at 40 °C to yield a powdery material (Table S1†). The precursor composite was then calcined in an electric furnace at 500 °C for 60 min in static air to yield an HE-MARIMO. Quaternary

Table 1 Solvothermal reactions under various solvent and additive conditions to obtain precursor composites[a]

| Entry | Solvent | Additive 1[b] | | Additive 2[b] | | Yield[c]/% |
		Material	Amount/mmol	Material	Amount/mmol	
1	MeOH	diEG	11.1	—	—	57
2	MeOH	triEG	11.1	—	—	59
3	10%MeOH/MeCN	triEG	1.75	—	—	96
4	10%MeOH/MeCN	triEG	3.50	—	—	102
5	10%MeOH/MeCN	triEG	5.25	—	—	94
6	10%MeOH/MeCN	triEG	7.00	—	—	72
7	10%MeOH/MeCN	tetraEG	5.25	—	—	106
8	10%MeOH/MeCN	acacH	5.25	—	—	135
9	10%MeOH/MeCN	triEG	5.25	acacH	5.25	119
10	10%MeOH/MeCN	triEG	5.25	BA	0.35	78
11	50%MeOH/MeCN	triEG	5.25	—	—	72
12	50%MeOH/MeCN	triEG	2.63	diEG	2.63	72

[a] Reaction conditions. Metal sources (0.07 mmol each): $Cr(NO_3)_3 \cdot 9H_2O$, $Mn(NO_3)_2 \cdot 6H_2O$, $Fe(NO_3)_3 \cdot 9H_2O$, $Co(NO_3)_2 \cdot 6H_2O$, and $Ni(NO_3)_2 \cdot 6H_2O$; solvent: 3.50 mL; ramp rate: 5.4 °C min^{-1}; temperature: 300 °C; time: 10 min. [b] diEG, triEG, tetraEG, acacH, and BA represent diethylene glycol, triethylene glycol, tetraethylene glycol, acetylacetone, and benzoic acid, respectively. [c] Calculated as trimetal tetraoxide (M_3O_4).

MARIMOs were similarly synthesized; reaction conditions are listed in Table S1.†

Preparation of a composite *via* solid-state synthesis

Cr_2O_3 (152 mg, 1.00 mmol), MnO_2 (174 mg, 2.00 mmol), Fe_2O_3 (160 mg, 1.00 mmol), Co_3O_4 (161 mg, 0.667 mmol), and NiO (149 mg, 2.00 mmol) were ground well in a mortar for 10 min until there was no color irregularity. The powder was then calcined at 500 °C for 60 min in static air to yield a solid-state synthesis (sss) composite.

Characterization

Transmission electron microscopy (TEM) images were acquired with a JEM-2100F (JEOL, Japan) microscope with an acceleration voltage of 200 kV and a JEM-ARM200F "NEO ARM" (JEOL) with an acceleration voltage of 200 kV. Scanning electron microscopy (SEM) images were acquired with an SU8020 microscope (Hitachi, Japan) with an acceleration voltage of 2 kV. Energy-dispersive X-ray spectroscopy (EDX) was performed with an INCA X-Max 80 (Oxford, UK) EDX spectrometer equipped with a TEM (JEM-2100F), a JED-2300T (JEOL) EDX spectrometer equipped with a TEM (JEM-ARM200F), and an INCA X-Max 80 (Oxford) EDX spectrometer equipped with an SEM (SU8020). X-ray diffraction (XRD) patterns were acquired with a SmartLab (Rigaku, Japan) diffractometer using nickel-filtered Cu-Kα radiation (1.5418 Å) with an acceleration voltage of 45 kV and a current of 200 mA in steps of 0.01 or 0.02° and a rate of 20° min^{-1} over the 2θ range of 10–70°. The crystallite sizes were estimated using Scherrer's equation, based on a peak of 440 diffraction around 63°. X-ray fluorescence (XRF) analyses were conducted using an Epsilon 1 (Malvern Panalytical, UK). Nitrogen adsorption/desorption isotherm measurements were performed with a BELSORP MINI X (MicrotracBEL, Japan), and the specific surface area was calculated by the Brunauer–Emmett–Teller (BET) method. The sample was pre-treated at 100 °C under vacuum for 60 min prior to the measurements. The RWGS reaction was performed using a BELCAT II (MicrotracBEL). X-ray photoelectron spectroscopy (XPS) was performed using an AXIS-HS (SHIMADZU-KRATOS, Japan) with an Al-Kα X-ray source (7 mA, 12 kV). Curve fitting of XPS spectra was carried out by using KolXPD software.

RWGS reaction

The calcined sample (30 mg) was loaded in a 7.5 mm-inner-diameter quartz tube and heated to 700 °C for 68 min under flowing Ar (50 sccm). Then, the RWGS reaction was conducted at 700 °C for 15 h under a mixed gas stream of H_2 (10 sccm), CO_2 (10 sccm), and Ar (30 sccm). The outlet gas was analyzed with a MicrotracBEL BELMASS online mass spectrometer.

Results and discussion

Survey of solvothermal reaction conditions to obtain precursor composites

Reaction conditions to obtain the precursor composites were surveyed using a small reactor (10 mL). Metal nitrates were used as metal sources because they are highly soluble in various solvents and residual nitrate anions can be easily removed by calcination. Solvents and additives were selected considering their solubilities and coordination abilities with metal ions. First, methanol that dissolved the inorganic metal salts was used as a solvent, and diEG or triEG additive was combined (entries 1 and 2 in Table 1). The aggregates consisting of large and irregularly shaped particles with scattered primary particles [Fig. 1a(i and ii)] were obtained. Then, acetonitrile was used as an alternative polar aprotic solvent because many spherical porous MARIMOs were obtained, as reported previously.[24] Unfortunately, solubilities of the inorganic salts in acetonitrile were low. Then, 10 vol% of methanol was mixed with acetonitrile (entries 3–10). In addition, the amounts of triEG were altered (entries 3–6). A small amount of triEG (1.75 mmol) produced spherical secondary particles with
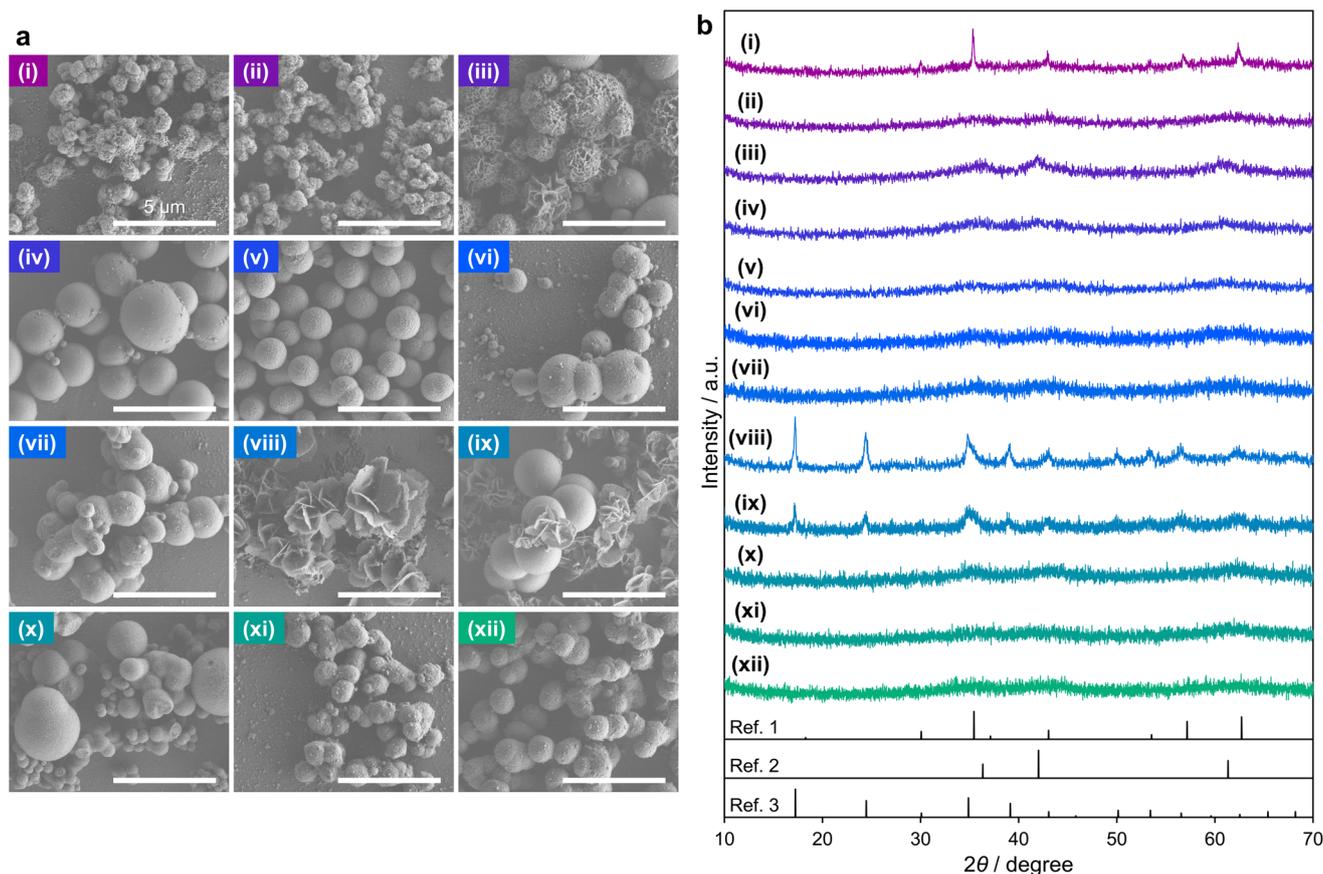
Fig. 1 SEM images (a) and XRD patterns (b) of products (i)–(xii) corresponding to entries 1–12 in Table 1, respectively. Scale bars of SEM images (a) are 5 μm. Black lines in (b), ref. 1, 2, and 3, correspond to reference diffraction peak positions of cubic Fe_3O_4 (PDF#00-001-1111), cubic FeO (PDF#00-001-1223), and cubic $Co(Fe(CN)_5NO)\cdot5H_2O$ (PDF#00-043-0768), respectively.

smooth or sheet-like surfaces, and the particle size was uneven [Fig. 1a(iii)]. The addition of 3.50 mmol of triEG resulted in spherical secondary particles with smooth surfaces and large and small sizes [Fig. 1a(iv)]. A larger amount of triEG (5.25 mmol) resulted in spherical particles with almost uniform sizes [Fig. 1a(v)]. However, increased amounts of triEG (7.00 mmol) led to irregular sizes [Fig. 1a(vi)]. Thus, 5.25 mmol of triEG produced the best results. Other additives, such as tetraEG, acacH, and BA, were used independently and/or combined with triEG. TetraEG resulted in agglomerates of spheres [Fig. 1a(vii)]. The combination of triEG and BA also yielded agglomerated spheres with a variety of particle sizes [Fig. 1a(x)]. When acacH was used, agglomerated spheres and agglomerates with flakes were obtained [Fig. 1a(viii and ix)], and their crystal structures were consistent with Co(Fe(CN)$_5$NO)·5H$_2$O [Fig. 1b(viii and ix)]. In addition, excessive methanol in methanol/acetonitrile mixed solvents (entries 11 and 12) resulted in products with rough surfaces [Fig. 1a(xi)], and smooth surfaces were not recovered by the addition of diEG [Fig. 1a(xii)].

Solvents would become subcritical fluids with lower polarity at the temperature region during the reaction. In such case, polar triEG and metal salts would be excluded from the less

polar solvent. Spherical morphology can be derived from minimizing the contact surface area of the polar materials with the outer less polar atmosphere (solvent) in the reaction, as can be seen in emulsification polymerization. Additives (triEG, acacH, *etc.*) can coordinate to metal cations and the surface of the primary and secondary particles, which would control the reaction (hydrolysis) speed of the metal compounds, direction of crystal growth, and/or aggregation of the yielded particles. triEG acted as a weak capping reagent of the particle surface, resulting in spherical particles.

Large-scale preparation of an HE-MARIMO

The solvothermal reaction was scaled-up ten-fold to obtain larger amounts of precursor composites. A 100 mL autoclave with a Teflon sleeve was used for the reaction, and the reaction temperature was limited to 200 °C because of the allowable operating temperature of the Teflon sleeve. The reaction time was instead extended to 30 min. Spherical secondary particles similar to those from the small-scale reaction were obtained with 109% yield (calculated as trimetal tetraoxide, M$_3$O$_4$) (Fig. 2a). The composite ratios of the metal elements were determined *via* XRF analysis (Table S2†). The five metal elements were present in almost equal amounts. TEM images
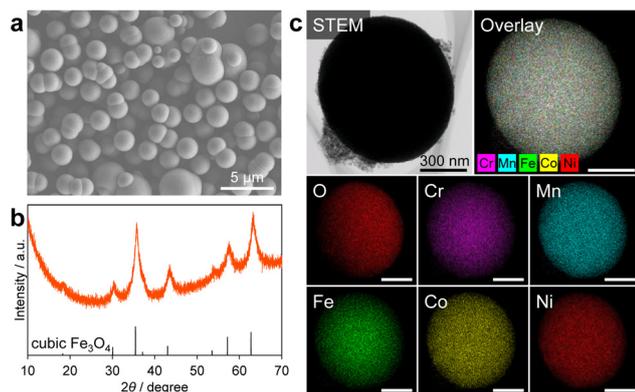
Fig. 2 SEM image of a precursor composite (before calcination, a). An XRD pattern (b), and STEM and EDX mappings (c) of HE–MARIMO (after calcination). The black lines in (b) correspond to reference diffraction peak positions of cubic Fe_3O_4 (PDF#00-001-1111). An overlay image in (c) created by merging EDX mapping images of Cr, Mn, Fe, Co, and Ni. Scale bars of STEM and EDX mapping images (c) are 300 nm.
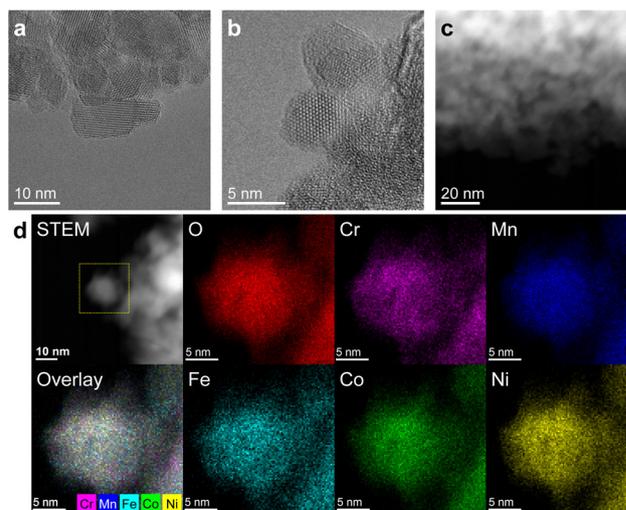

Fig. 3 High-resolution TEM images (a and b), HAADF-STEM image (c), and STEM and EDX mappings (d) of HE–MARIMO. An overlay image in (d) created by merging EDX mapping images of Cr, Mn, Fe, Co, and Ni.

of the precursor composites indicated that spherical particles were formed from small primary particles (Fig. S1a†), and scanning TEM (STEM)/EDX analysis revealed homogeneous and fine distributions of the five elements in the spheres (Fig. S1b†). The XRD pattern of the precursor composite was an amorphous broad profile (Fig. S2†). Thus, the solvo-thermal-reaction-prepared precursor composite was calcined at 500 °C for 60 min in air to remove organic residues and increase the crystallinity, and an HE-MARIMO was obtained. The color of the precursor composite was initially dark brown and then changed to black after calcination. The crystal structure via XRD of the calcined product (HE-MARIMO) was consistent with a single-phase spinel structure like cubic Fe_3O_4 (Fig. 2b). Based on XRD, the HE-MARIMO crystallites were as small as 6 nm, and the BET specific surface area was 46 m^2 g^{-1} (Fig. S3a†). HE-MARIMO maintained a spherical second-order structure even after calcination (Fig. 2c). Fig. S1b† and Fig. 2c respectively show STEM and EDX mapping images of the precursor composite and the HE-MARIMO, where the Cr, Mn, Fe, Co, and Ni components were homogeneously dispersed throughout the sphere at the nanoscale.

The nanostructure of HE-MARIMO was investigated in detail via atomic-resolution analytical TEM (Fig. 3). For the analysis, HE-MARIMO was ground with an agate mortar. Primary particles with ca. 20 nm and <5 nm sizes were observed on the surface and in the HE-MARIMO cross-section (Fig. 3a and b). A high-angle annular dark field (HAADF)-STEM image of the surface revealed the porous structure (Fig. 3c). In addition, the metal distributions at the primary particle level via STEM/EDX analysis indicated that the five metals were homogeneously mixed (Fig. 3d). Thus, based on XRD patterns and STEM/EDX analyses, the HE-MARIMO formed a high-entropy oxide with a single-phase spinel structure.

As a comparison, an sss-composite metal oxide was prepared by standard solid-state synthesis with Cr_2O_3, MnO_2,

Fe_2O_3, Co_3O_4, and NiO source materials, followed by calcination under the same conditions as that for HE-MARIMO (500 °C and 60 min). An XRD pattern and TEM and STEM/EDX images of the sss-composite are shown in Fig. S4 and S5.† The XRD pattern (Fig. S4†) exhibited many peaks corresponding to the source metal oxides indicating that the product was not homogeneously mixed under such mild conditions. TEM images (Fig. S5a†) showed particles with different shapes and sizes. STEM/EDX analysis (Fig. S5b†) indicated that the five elements were unevenly distributed and not well mixed. Thus, the sss-composite prepared via the solid-state synthetic method did not yield a single-phase solid solution of the five oxides when calcined at 500 °C for 60 min, while HE-MARIMO did yield the solid solution under the same conditions. Small nanoparticles would migrate more easily than large particles because of their higher surface energy, and atom diffusion between the nanoparticles would be rapid. Because the five metals in the HE-MARIMO precursor composite were homogeneously mixed at the nanoscale and the primary particles were small, HE-MARIMO could be obtained via low-temperature approaches.

RWGS reaction catalyzed by HE-MARIMO

HE-MARIMO is a mixed spinel oxide containing 3d elements which is known to act as a catalyst for the RWGS reaction. It was expected to have high structural and thermal stabilities attributed to the HEO properties. Therefore, the RWGS reaction was performed and the HE-MARIMO catalytic activity and stability were compared with those of the sss-composite. Fig. 4a–d show the results of the RWGS reaction at 700 °C for 15 h using HE-MARIMO and the sss-composite as catalysts. Under these conditions, the CO_2 conversion equilibrium was at 44.0%. HE-MARIMO exhibited a higher CO_2 conversion and CO yield than the sss-composite. The highest CO_2 conversion
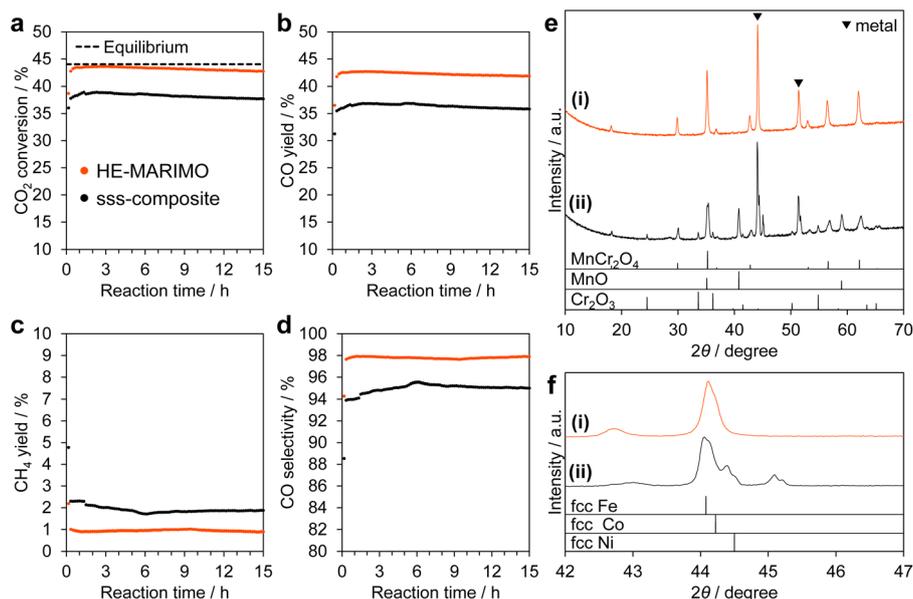
Fig. 4 Catalytic performance of HE-MARIMO and the sss-composite for the RWGS reaction. CO_2 conversion (a), CO yield (b), CH_4 yield (c), and CO selectivity (d) at 700 °C for 15 h (H_2/CO_2 ratio of 1 : 1). XRD patterns (e and f) of the spent HE-MARIMO (i) and the sss-composite (ii). (f) is an enlarged view of the 42–47° range shown in (e). Peaks marked by inverted triangles in (e) are derived from some metal species. Black lines in (e) correspond to reference diffraction peak positions of cubic $MnCr_2O_4$ (PDF#00-054-0876), cubic MnO (PDF#01-075-0625), and hexagonal Cr_2O_3 (PDF#01-082-1484). Black lines in (f) correspond to reference diffraction peak positions of fcc Fe (PDF#01-081-8771), fcc Co (PDF#00-015-0806), and fcc Ni (PDF#00-004-0850).

for HE-MARIMO was 43.6%, which was almost the equilibrium maximum, and the CO_2 conversion decreased by only 0.9% over 15 h, indicating excellent durability. In addition, the CH_4 by-product yield was as low as 1% and stable over 15 h, resulting in a 98% CO selectivity. For the reference sss-composite, however, the CH_4 yield fluctuated over time. Thus, HE-MARIMO exhibited superior catalytic activity and stability in the RWGS reaction.

Long-time cycle tests were performed since the catalytic activity of HE-MARIMO was close to equilibrium and there was little decrease in activity during the 15 h RWGS reaction. The RWGS reaction was repeated three times at 700 °C for 20 h using HE-MARIMO as a catalyst (Fig. S6†). In the 1st cycle, the CO_2 conversion was close to equilibrium during *ca.* 10 h. However, the catalytic activity gradually decreased, and the initial activity in the 2nd cycle was about 40%. The CO_2 conversion (*ca.* 40%) was maintained throughout the 2nd and 3rd cycles. HE-MARIMO was used as a catalyst for the RWGS reaction at high temperatures for a total of 60 h, and even in the 3rd cycle, the catalytic activity was slightly higher than the initial activity of the sss-composite. Thus, HE-MARIMO has excellent catalytic activity and durability.

To understand the catalytic performances of the HE-MARIMO and sss-composites, XRD patterns of the spent catalysts were collected. Fig. 4e shows the XRD patterns after the RWGS reaction at 700 °C for 15 h. Several peaks consistent with the spinel structure at positions close to $MnCr_2O_4$ and high-intensity peaks (44 and 52°, marked by inverted triangles) attributed to some metals can be seen in the XRD pattern of

the spent HE-MARIMO. In contrast, the XRD pattern of the spent sss-composite displayed several peaks consistent with a spinel structure and some metals, as well as peaks corresponding to rock-salt structures similar to MnO and corundum structures similar to Cr_2O_3. The intensity of the peak derived from the metals (44°) was the highest, the intensities of the spinel ($MnCr_2O_4$) and rock-salt (MnO) phases were similar, and the intensity of the peaks consistent with corundum (Cr_2O_3) was the lowest. Expansion of the area around 44° in Fig. 4e is shown in Fig. 4f. The spent HE-MARIMO had one peak with a small shoulder, while the spent sss-composite had several peaks, indicating that almost a single metal component was generated during the RWGS reactions with HE-MARIMO, while several were generated in the sss-composite. The positions of the new peaks were similar to those of fcc Fe, fcc Co, and fcc Ni. However, several metals may be mixed and it is not possible to determine by XRD which metals have been phase-separated. Therefore, elemental distributions of the spent catalysts were investigated.

TEM analyses of the spent catalysts

TEM/EDX analyses of the spent HE-MARIMO are shown in Fig. 5a–d, where large agglomerates were formed on the spheres and the HE-MARIMO primary particle size increased. The STEM/EDX analysis of HE-MARIMO (Fig. 5d and S7†) exhibited agglomerates of Co and Ni with Fe on the spheres. Cr and Mn were highly dispersed and distributed at the same sites as O, suggesting that Cr and Mn still existed as spinel oxides. In contrast, the locations of Co and Ni in the EDX
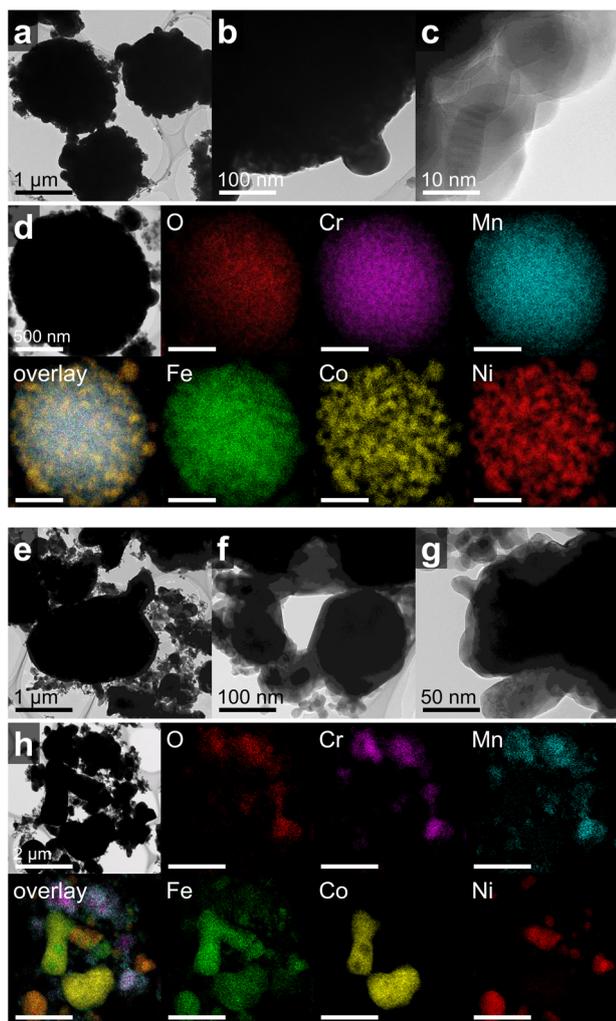
Fig. 5 TEM images (a–c), STEM and EDX mapping images (d) of the spent HE-MARIMO. Scale bars of EDX mapping images (d) are 500 nm. TEM images (e–g), and STEM and EDX mapping images (h) of spent sss-composite. Scale bars of EDX mapping images (h) are 2 μm.

only partially matched that of O to a small degree. The distributions Co and Ni also did not overlap with that of O. In EDX mapping distributions of Fe, Co, and Ni, various aggregates of Fe/Co and Fe/Ni were present. These STEM/EDX results were consistent with the XRD analysis of the spent catalyst. Therefore, the sharp metal peak at 44 and 52° in Fig. 4e in spent HE-MARIMO was attributed to Co–Ni alloys containing Fe, and the metal peaks in the spent sss-composite were attributed to Fe–Co alloys, Fe–Ni alloys, *etc*. The phase separation of a single-type alloy (Co–Ni alloys containing Fe) in HE-MARIMO could be attributed to the homogeneity of the five metals prior to the catalysis. Conversely, the heterogeneity of the sss-composite could lead to the formation of various Fe-based alloys with Co and Ni because of the smaller Fe particle sizes based on TEM images before catalysis (Fig. S5†).

Preparation of quaternary MARIMOs with four metal elements

To investigate the active species and the role of each element in the RWGS reaction, quaternary MARIMOs were synthesized with one element missing and applied to the RWGS reaction. As shown in Table S1,† the five quaternary MARIMOs (Cr-free, Mn-free, Fe-free, Co-free, and Ni-free) were prepared using a procedure similar to that for HE-MARIMO. All precursor composites prepared *via* the solvothermal reaction had a dark brown color that changed to black after calcination in air. The XRF analyses revealed that four metals were almost equally present in the products (Table S2†). Fig. 6 shows SEM images of the precursor composites (before calcination) and the XRD patterns of the calcined products (quaternary MARIMOs). Spherical secondary particles like HE-MARIMO were mainly obtained, although the secondary particle sizes, size distributions, and degrees of aggregation of the secondary particles were different. The different types of transition-metal salts have inherently different reactivity. These differences in morphologies and particle sizes are due to the differences in the reactivity of each metal salt and its interaction with ligands
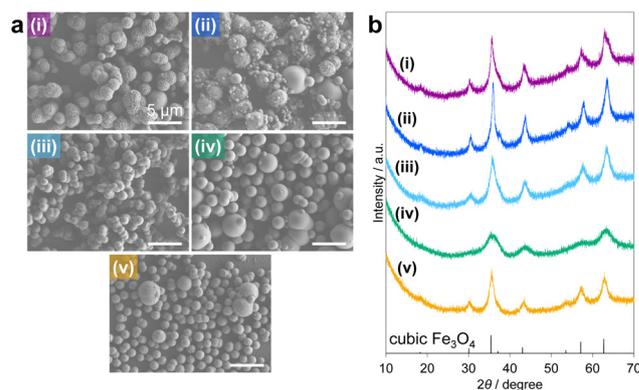
mapping distributions differed from those of O, indicating that Co–Ni alloys were formed. Because the EDX mapping of Fe overlapped with similar positions of both O and Co–Ni alloys, Fe existed as both a spinel oxide and an alloy. Thermal reduction yielding Co–Ni alloys with Fe would be dominant because of the higher redox potentials (Table S3†) of Fe (−0.440 V), Co (−0.277 V), and Ni (−0.257 V) relative to Cr (−0.90 V) and Mn (−1.18 V).

For the sss-composite, dispersed distributions of elements were observed in STEM/EDX mappings (Fig. 5h and S8†). In Fig. 5h and S8b,† Cr and Mn were located at sites similar to O in the EDX mapping. However, as seen in the overlay image, the Cr and Mn distributions did not match completely. Also, Fig. S8a† shows that the Cr and Mn distributions did not match at all. This could be explained by the presence of a variety of oxide, spinel, rock-salt, and corundum structures observed in the XRD data (Fig. 4e(ii)). The distribution of Fe

Fig. 6 SEM images (a) of precursor composites (before calcination) and XRD patterns (b) of quaternary MARIMOs (after calcination). (i–v) correspond to Cr-free, Mn-free, Fe-free, Co-free, and Ni-free MARIMOs, respectively. Scale bars of SEM images (a) are 5 μm. The black lines in (b) correspond to reference diffraction peak positions of cubic Fe_3O_4 (PDF#00-001-1111).
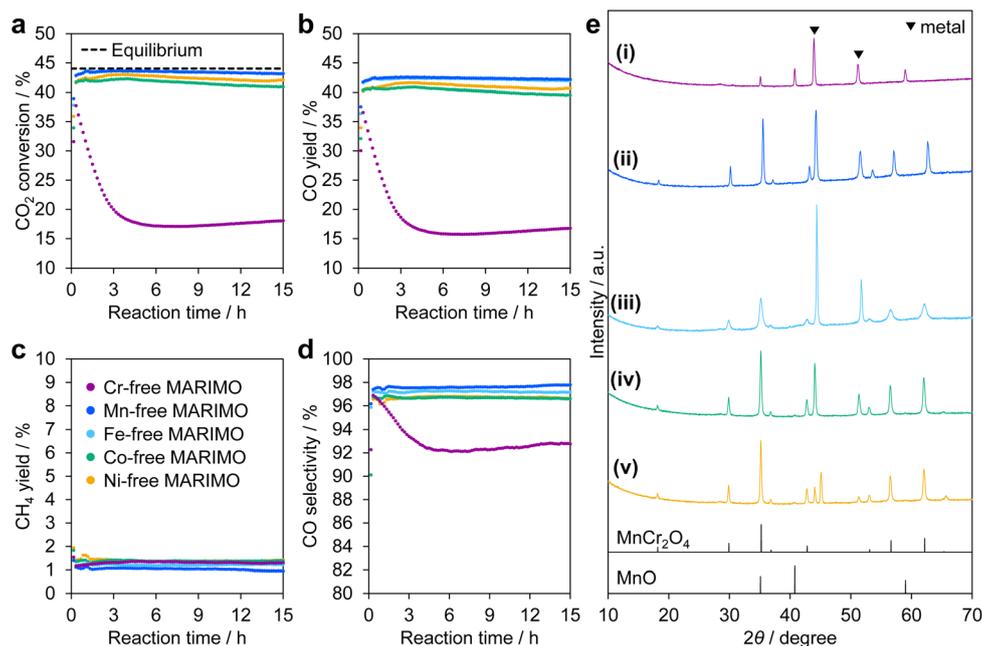
Fig. 7 Catalytic performance of quaternary MARIMOs in the RWGS reaction. CO_2 conversion (a), CO yield (b), CH_4 yield (c), and CO selectivity (d) at 700 °C for 15 h (H_2/CO_2 ratio of 1 : 1). XRD patterns (e) of spent catalysts. Cr-free (i), Mn-free (ii), Fe-free (iii), Co-free (iv), and Ni-free MARIMOs (v). Peaks marked by inverted triangles in (e) are derived from some metal species. Black lines in (e) correspond to reference diffraction peak positions of $MnCr_2O_4$ (PDF#00-054-0876) and cubic MnO (PDF#01-075-0625).

(solvents and additives). In the quaternary MARIMOs with different elemental compositions, the reaction rate and particle formation process in the solvothermal reactions can be different, which would change the morphologies and sizes of the yielded particles. The XRD patterns of the quaternary MARIMOs were consistent with the spinel structure, and the crystallites were as small as <8 nm (Table S2†). Co-free MARIMO had the smallest crystallites at 2.9 nm. Thus, quaternary MARIMOs with properties similar to HE-MARIMO were prepared.

RWGS reactions catalyzed by quaternary MARIMOs

Fig. 7a–d show the difference in the catalytic performance between Cr-free and the other quaternary MARIMOs. The initial catalytic activity of Cr-free MARIMO was about 40%, which is similar to that of other quaternary MARIMOs and HE-MARIMO. However, the catalytic activity of Cr-free MARIMO was decreased significantly within 3 h, after which the CO_2 conversion remained below 20%. Whereas the Mn-free, Fe-free, Co-free, and Ni-free MARIMOs exhibited higher catalytic activities and stabilities similar to those of HE-MARIMO over 15 h. Their catalytic activities were all higher than that of the sss-composite, and the CH_4 yields were as low as 1% for all the catalysts. The CO selectivity of Cr-free MARIMO was lower than that of the other MARIMOs because of the low CO yield. In contrast, the other MARIMOs exhibited higher CO selectivity. Hence, Cr was a critical catalytic component in terms of stabilization. The quaternary MARIMO catalysts exhibited almost the same high activity as HE-MARIMO

when Cr was present (an enlarged view of CO_2 conversion is shown in Fig. S9†). Mn-free MARIMO and Fe-free MARIMO showed slightly higher activity than HE-MARIMO. However, our purpose is not to prepare the highest-performing catalyst but to develop a new synthetic method for HEOs, and therefore this does not mean that HE-MARIMO loses its value.

To investigate the role of each element, the crystal structures of the spent catalysts were analyzed by XRD (Fig. 7e). XRD patterns of Mn-free, Fe-free, Co-free, and Ni-free MARIMOs exhibited peaks consistent with the spinel structure like $MnCr_2O_4$ as well as metal peaks (around 44 and 52°). These results were similar to those for HE-MARIMO, although the peak intensity ratio of 35° (spinel) to 44° (metal) varied from sample to sample. The differences in peak intensity ratios may be due to the degree of sintering of the spinel crystal and the amount and the crystallinity of phase-separated metal species (Table S4† summarizes the crystallite sizes of the spent MARIMOs). The XRD pattern of the spent Cr-free MARIMO also had a high-intensity metal peak similar to those for the other spent MARIMOs. However, there was no peak attributed to the spinel structure; instead, there were peaks consistent with cubic MnO (rock-salt structure). Thus, Cr significantly contributed to the stabilization of the spinel structure. Some of the spinel oxides are known as active species in the RWGS reaction due to their divalent/trivalent redox couples in metal elements.[46–48] Therefore, the significant deactivation of Cr-free MARIMO in the RWGS reaction could be attributed to the change from the active spinel structure to the less-active rock-salt structure. Based on the XRD peak posi-

tions, the four Cr-containing quaternary MARIMOs (Mn-free, Fe-free, Co-free, and Ni-free MARIMOs) had different types of phase-separated metal components, but with similar catalytic activities. Moreover, they maintained the catalytic activity for at least 15 h, despite the phase separation of the metal components. These results thus indicated that the spinel oxides could be the active site as well. The results of the catalytic test of the quaternary MARIMOs showed that inclusion of Cr in the oxides lengthened the catalytic activity even without one of the other elements (Mn, Fe, Co, and Ni).

SEM/EDX analyses of the spent quaternary MARIMOs were performed to determine which metal species were phase-separated from the spinel oxides during the RWGS reaction. The separated metal species from Cr-free MARIMO and other MARIMOs were completely different. The original spherical morphology was not maintained in the case of Cr-free MARIMO after the RWGS reaction (Fig. S10†). The fused material clinging to the spherical particles was seen, which can be Co–Ni alloys with Fe based on EDX mapping images. The separation of Co and Ni from O and Mn was observed, and Fe was distributed in both. The composition of the separated metal species was similar to HE-MARIMO (Fig. 5d). The SEM image of the spent Cr-free MARIMO showed large lumps of alloys, however metal peaks of the XRD pattern were not so large and the crystallite size was 41 nm [Fig. 7e(i)], then the large lumps would be polycrystalline.

In contrast, small aggregates were observed on the surface of the other spent MARIMOs (Fig. S11–S14†) as well as spent HE-MARIMO. Based on EDX analyses of the spent Mn-free MARIMO (Fig. S11†), the aggregates were Co–Ni alloys. EDX mapping images showed that Cr and Fe had a similar distribution as O, and that Co and Ni formed small aggregates on the spheres. However, different from the spent Cr-free MARIMO, Co and Ni were also distributed on spheres. The elemental distributions of spent Fe-free MARIMO (Fig. S12†) were similar to that of Mn-free MARIMO, and aggregation of Co and Ni was observed. In the spent Co-free MARIMO (Fig. S13†), aggregation of only Ni was observed, suggesting that the metal peaks in the XRD pattern [Fig. 7e(iv)] correspond to metallic Ni. In Ni-free MARIMO (Fig. S14†), aggregation of Co and Mn was observed; however their location did not match, indicating no formation of Mn–Ni alloys. Throughout, Cr-free MARIMO shows a different degree of metal separation compared to other MARIMOs. Cr would stabilize the spinel structure and improve the thermal resistance. The similar effect of Cr on the stabilization of $FeCr_2O_4$ and $ZnCr_2O_4$ with a spinel structure was known,[46,49] and the phenomenon was also demonstrated in this study.

XPS analyses of HE-MARIMO and Cr-free MARIMO before and after the RWGS reaction were conducted to investigate the oxidation state of each metal. Fig. S15† shows XPS spectra of each element in HE-MARIMO before use; the curve fitting indicated the existence of Cr^{3+}, Cr^{6+}, Mn^{3+}, Mn^{4+}, Fe^{2+}, Fe^{3+}, Co^{2+}, Co^{3+}, Ni^{2+}, and Ni^{3+} in HE-MARIMO. The variation of valence states of each metal element revealed that HE-MARIMO had not a normal or inverse spinel structure but a mix spinel struc-

ture with five metal elements randomly occupying both tetragonal and octahedral sites. According to the literature, the mix and inverse spinel structures possess more oxygen vacancies that promote the RWGS reaction.[47] XPS spectra of Cr-free MARIMO also showed the various valence states of each metal element (Fig. S16†) similar to HE-MARIMO before use. The profiles of XPS spectra of HE-MARIMO and Cr-free MARIMO before use as catalysts were similar, while spectra of spent HE-MARIMO and Cr-free MARIMO were different.

Fig. S17† shows the XPS spectra of spent HE-MARIMO. In the Cr 2p spectrum, the peak area of Cr^{6+} was decreased compared with that before use. The Mn 2p spectrum includes small deconvolution peaks attributable to Mn^{2+} in addition to Mn^{3+} and Mn^{4+}. The Fe 2p spectrum did not change much before and after the reaction, indicating the presence of both Fe^{2+} and Fe^{3+}. In the Co 2p spectrum, the Co^{3+} peak area decreased and the Co^{2+} peak area increased. The peaks attributable to metallic Co were negligible, indicating that Co was present mainly as metal oxides, though Co–Ni alloys were formed. The Ni 2p spectrum includes small deconvolution peaks attributable to metallic Ni together with Ni^{2+} and Ni^{3+}. The Ni^{2+} peak area decreased significantly and the Ni^{3+} peak area increased after use. Judging from the peak areas of Ni, Ni^{2+}, and Ni^{3+}, Ni species were present mainly as oxides.

Fig. S18† shows the XPS spectra of spent Cr-free MARIMO. The Mn 2p spectrum includes large deconvolution peaks attributable to Mn^{2+} with peaks of Mn^{3+} and Mn^{4+}. The presence of Mn^{2+} would relate to the rock-salt structure shown in the XRD pattern. The intensity of the Co 2p spectrum was low, but the metallic Co probably existed with Co^{2+} and Co^{3+}. A clear peak corresponding to metallic Ni was present in the Ni 2p spectrum. The relative peak intensity of metallic Ni of the spent Cr-free MARIMO was clearly different from that of the spent HE-MARIMO. The oxidation state of HE-MARIMO did not change significantly before and after the RWGS reaction. Only a small amount of Ni species was detected. In contrast, many reduced elements such as Mn^{2+}, Co, and Ni were detected in the spent Cr-free MARIMO. Therefore, the incorporated Cr could contribute to the inhibition of metal species by the stabilization of the spinel structure.

Two types of reaction mechanisms, redox and associative mechanisms, were discussed for the catalytic RWGS reaction. Gu *et al.* revealed that a Cu-modified iron oxide with a spinel structure catalyzed the RWGS reaction *via* the redox mechanism.[50] Bahmanpour *et al.* revealed that carbonate species were formed on the surface of the $CuAl_2O_4$ spinel and the $CoAl_2O_4$ spinel during the RWGS reaction.[47] In both reaction mechanisms, oxygen vacancies play an important role by providing an adsorption site for CO_2. HE-MARIMO had a mix spinel structure with oxygen vacancies based on the XPS analysis. The presence of oxygen vacancies would be one of the reasons why HE-MARIMO showed high catalytic activity for the RWGS reaction. In addition, materials that spontaneously form a phase-separated structure (metal and oxide) by reaction are known to be highly active and resistant due to a large number of active sites (metal–oxide interfaces).[51] The highly

homogeneous distribution of metal species in HE-MARIMO resulted in the formation of Co–Ni alloys inside the spherical particles during the RWGS reaction, as seen in the STEM/EDX images (Fig. 5d). This phase-separated structure may contribute to the high activity of HE-MARIMO.

Conclusions

High-entropy $(Co_{0.2}Cr_{0.2}Fe_{0.2}Mn_{0.2}Ni_{0.2})_3O_4$ MARIMO was synthesized *via* a two-step process involving a solvothermal reaction followed by calcination. The HE-MARIMO had a single-phase spinel crystal structure with crystallite sizes as small as 6 nm. The formation of the single-phase spinel structure *via* low-temperature and short-duration calcination at 500 °C for 60 min was attributed to the formation of the homogeneous precursor composite at the nanometer level *via* the solvothermal reaction. The HE-MARIMO exhibited excellent catalytic activity, CO selectivity, and stability during the RWGS reaction at 700 °C for 15 h. The Cr contribution to the stabilized spinel structure was revealed. The catalytic activity of HE-MARIMO was higher than that of the sss-composite prepared *via* solid-state synthesis. Overall, this work demonstrated the advantage of the solvothermal method in the synthesis of high-entropy oxides, which can be used for other high-entropy materials.

Author contributions

Ayano Taniguchi: conceptualization, data curation, formal analysis, funding acquisition, investigation, methodology, visualization, writing – original draft, and writing – review & editing. Takeshi Fujita: data curation and formal analysis. Kazuya Kobiro: funding acquisition, project administration, resources, supervision, and writing – review & editing.

Conflicts of interest

There are no conflicts to declare.

Acknowledgements

References

1 B. Cantor, I. T. H. Chang, P. Knight and A. J. B. Vincent, *Mater. Sci. Eng., A*, 2004, **375–377**, 213–218.

2 J.-W. Yeh, S.-K. Chen, S.-J. Lin, J.-Y. Gan, T.-S. Chin, T.-T. Shun, C.-H. Tsau and S.-Y. Chang, *Adv. Eng. Mater.*, 2004, **6**, 299–303.

3 A. Sarkar, Q. Wang, A. Schiele, M. R. Chellali, S. S. Bhattacharya, D. Wang, T. Brezesinski, H. Hahn, L. Velasco and B. Breitung, *Adv. Mater.*, 2019, **31**, 1806236.

4 E. Lewin, *J. Appl. Phys.*, 2020, **127**, 160901.

5 Y. Wang, *Adv. Appl. Ceram.*, 2022, **121**, 57–78.

6 Y. Zhang, W.-M. Guo, Z.-B. Jiang, Q.-Q. Zhu, S.-K. Sun, Y. You, K. Plucknett and H.-T. Lin, *Scr. Mater.*, 2019, **164**, 135–139.

7 M. Anandkumar and E. Trofimov, *J. Alloys Compd.*, 2023, **960**, 170690.

8 J. Zhang, J. Yan, S. Calder, Q. Zheng, M. A. McGuire, D. L. Abernathy, Y. Ren, S. H. Lapidus, K. Page, H. Zheng, J. W. Freeland, J. D. Budai and R. P. Hermann, *Chem. Mater.*, 2019, **31**, 3705–3711.

9 D. Wang, S. Jiang, C. Duan, J. Mao, Y. Dong, K. Dong, Z. Wang, S. Luo, Y. Liu and X. Qi, *J. Alloys Compd.*, 2020, **844**, 156158.

10 Z. Grzesik, G. Smola, M. Miszczak, M. Stygar, J. Dabrowa, M. Zajusz, K. Swierczek and M. Danielewski, *J. Eur. Ceram. Soc.*, 2020, **40**, 835–839.

11 A. Sarkar, L. Velasco, D. Wang, Q. Wang, G. Talasila, L. de Biasi, C. Kuebel, T. Brezesinski, S. S. Bhattacharya, H. Hahn and B. Breitung, *Nat. Commun.*, 2018, **9**, 1–9.

12 M. R. Chellali, A. Sarkar, S. H. Nandam, S. S. Bhattacharya, B. Breitung, H. Hahn and L. Velasco, *Scr. Mater.*, 2019, **166**, 58–63.

13 A. H. Phakatkar, M. T. Saray, G. M. Rasul, L. V. Sorokina, T. G. Ritter, T. Shokuhfar and R. Shahbazian-Yassar, *Langmuir*, 2021, **37**, 9059–9068.

14 J. Yang, J. Zhang, B. Zou, H. Zhang, J. Wang, U. Schubert and Y. Rui, *ACS Appl. Nano Mater.*, 2020, **3**, 4265–4273.

15 Y. Zhu, G. Seong, T. Noguchi, A. Yoko, T. Tomai, S. Takami and T. Adschiri, *ACS Appl. Energy Mater.*, 2020, **3**, 4305–4319.

16 X. Yang, H. Wang, Y. Song, K. Liu, T. Huang, X. Wang, C. Zhang and J. Li, *ACS Appl. Mater. Interfaces*, 2022, **14**, 26873–26881.

17 S. K. Shaw, A. Gangwar, A. Sharma, S. K. Alla, S. Kavita, M. Vasundhara, S. S. Meena, P. Maiti and N. K. Prasad, *J. Alloys Compd.*, 2021, **878**, 160269.

18 S. L. Fereja, Z. Zhang, Z. Fang, J. Guo, X. Zhang, K. Liu, Z. Li and W. Chen, *ACS Appl. Mater. Interfaces*, 2022, **14**, 38727–38738.

19 X. Hao, A. Yoko, C. Chen, K. Inoue, M. Saito, G. Seong, S. Takami, T. Adschiri and Y. Ikuhara, *Small*, 2018, **14**, 1802915.

20 L. Han, R. Liu, C. Li, H. Li, C. Li, G. Zhang and J. Yao, *J. Mater. Chem.*, 2012, **22**, 17079–17085.

21 Y. Xie, J. Chen, X. Wu, J. Wen, R. Zhao, Z. Li, G. Tian, Q. Zhang, P. Ning and J. Hao, *ACS Catal.*, 2022, **12**, 10587–10602.

22 H. T. T. Nguyen, T. Habu, M. Ohtani and K. Kobiro, *Eur. J. Inorg. Chem.*, 2017, **2017**, 3017–3023.

23 F. Duriyasart, A. Irizawa, K. Hayashi, M. Ohtani and K. Kobiro, *ChemCatChem*, 2018, **10**, 3392–3396.

24 A. Taniguchi, Y. Kumabe, K. Kan, M. Ohtani and K. Kobiro, *RSC Adv.*, 2021, **11**, 5609–5617.

25 Y. Kumabe, H. Taga, K. Kan, M. Ohtani and K. Kobiro, *RSC Adv.*, 2020, **10**, 14630–14636.

26 A. Taniguchi, R. Miyata, M. Ohtani and K. Kobiro, *RSC Adv.*, 2022, **12**, 22902–22910.

27 K. Wang, W. Hua, X. Huang, D. Stenzel, J. Wang, Z. Ding, Y. Cui, Q. Wang, H. Ehrenberg, B. Breitung, C. Kuebel and X. Mu, *Nat. Commun.*, 2023, **14**, 1487.

28 Y. Dang, Z. Xu, H. Yang, K. Tian, Z. Wang, R. Zheng, H. Sun, Y. Liu and D. Wang, *Appl. Surf. Sci.*, 2023, **636**, 157856.

29 H. Yang, L. He, Z. Yang, Q. Chen, G. Jiang, J. Zhu, R. Xue, N. Qiu and Y. Wang, *J. Alloys Compd.*, 2023, **968**, 172135.

30 Y.-Q. Wang, H.-M. Wang, Y.-C. Jiang, G.-R. Li, S. Liu and X.-P. Gao, *ACS Appl. Energy Mater.*, 2023, **6**, 8377–8387.

31 D. Wang, C. Duan, Y. Yu, X. Li, Z. Wang, Y. Liu and C. Liu, *J. Alloys Compd.*, 2023, **967**, 171758.

32 J. Du, X. Zhang, F. He and Y. Xie, *Electrochim. Acta*, 2023, **461**, 142599.

33 D. Wang, C. Duan, H. He, Z. Wang, R. Zheng, H. Sun, Y. Liu and C. Liu, *J. Colloid Interface Sci.*, 2023, **646**, 89–97.

34 M. V. Kante, M. L. Weber, S. Ni, I. C. G. van den Bosch, E. van der Minne, L. Heymann, L. J. Falling, N. Gauquelin, M. Tsvetanova, D. M. Cunha, G. Koster, F. Gunkel, S. Nemšák, H. Hahn, L. V. Estrada and C. Baeumer, *ACS Nano*, 2023, **17**, 5329–5339.

35 R. R. Katzbaer, F. M. dos Santos Vieira, I. Dabo, Z. Mao and R. E. Schaak, *J. Am. Chem. Soc.*, 2023, **145**, 6753–6761.

36 D. Chen, S. Nie, L. Wu, X. Zheng, S. Du, X. Duan, Q. Niu, P. Zhang and S. Dai, *Chem. Mater.*, 2022, **34**, 1746–1755.

37 J. Zhao, J. Bao, S. Yang, Q. Niu, R. Xie, Q. Zhang, M. Chen, P. Zhang and S. Dai, *ACS Catal.*, 2021, **11**, 12247–12257.

38 Y. Liao, Y. He, X. Cui and L. Liu, *Fuel*, 2024, **355**, 129494.

39 Q.-Y. Liu, C. Shang and Z.-P. Liu, *J. Phys. Chem. Lett.*, 2022, **13**, 3342–3352.

40 H. Xu, Y. Li, X. Luo, Z. Xu and J. Ge, *Chem. Commun.*, 2017, **53**, 7953–7956.

41 M. Zhu, Q. Ge and X. Zhu, *Trans. Tianjin Univ.*, 2020, **26**, 172–187.

42 R. Tang, Z. Zhu, C. Li, M. Xiao, Z. Wu, D. Zhang, C. Zhang, Y. Xiao, M. Chu, A. Genest, G. Rupprechter, L. Zhang, X. Zhang and L. He, *ACS Mater. Lett.*, 2021, **3**, 1652–1659.

43 L. Li, S. Miyazaki, S. Yasumura, K. W. Ting, T. Toyao, Z. Maeno and K.-i. Shimizu, *ACS Catal.*, 2022, **12**, 2639–2650.

44 E. Frei, A. Gaur, H. Lichtenberg, C. Heine, M. Friedrich, M. Greiner, T. Lunkenbein, J.-D. Grunwaldt and R. Schlögl, *ChemCatChem*, 2019, **11**, 1587–1592.

45 E. Gioria, P. Ingale, F. Pohl, R. N. d'Alnoncourt, A. Thomas and F. Rosowski, *Catal. Sci. Technol.*, 2022, **12**, 474–487.

46 S.-W. Park, O.-S. Joo, K.-D. Jung, H. Kim and S.-H. Han, *Korean J. Chem. Eng.*, 2000, **17**, 719–722.

47 A. M. Bahmanpour, F. Heroguel, M. Kilic, C. J. Baranowski, P. Schouwink, U. Rothlisberger, J. S. Luterbacher and O. Krocher, *Appl. Catal., B*, 2020, **266**, 118669.

48 J. C. Navarro, C. Hurtado, M. Gonzalez-Castano, L. F. Bobadilla, S. Ivanova, F. L. Cumbrera, M. A. Centeno and J. A. Odriozola, *J. CO₂ Util.*, 2023, **68**, 102356.

49 O. Yalcin, I. E. Wachs and I. Onal, *Int. J. Hydrogen Energy*, 2021, **46**, 17154–17162.

50 M. Gu, S. Dai, R. Qiu, M. E. Ford, C. Cao, I. E. Wachs and M. Zhu, *ACS Catal.*, 2021, **11**, 12609–12619.

51 H. Nishiguchi, A. S. B. M. Najib, X. Peng, Y. Cho, A. Hashimoto, S. Ueda, T. Fujita, M. Miyauchi and H. Abe, *Adv. Sustainable Syst.*, 2020, **4**, 2000041.